On the aerodynamic and aeroacoustic characteristics of a NACA 65-410 airfoil at moderate Reynolds number

B. Zang*, Yannick D. Mayer† and Mahdi Azarpeyvand‡

Faculty of Engineering, University of Bristol, United Kingdom

The present study investigates the flow dynamics and self-noise generated by a highly instrumented NACA 65-410 airfoil, which aims to provide a better understanding of the near-field aerodynamic and aeroacoustic characteristics and their correlation with airfoil noise. The experiments have been carried out in an aeroacoustic wind tunnel at two moderate Reynolds numbers, Re_c = 422,000 and 633,000 respectively. By varying the airfoil angle of attack through -2° to 15°, the flow transits from attached to fully separated (*i.e.* stall). The results have shown that the magnitude of the power spectral density (PSD) of the surface pressure fluctuations grows with increasing angle of attack, and furthermore a clear distinction exists between attached and separated flow characteristics. Furthermore, the near-field coherence between the chord-wise microphones revealed the development of large-scale structures convecting across the chord length of the airfoil as the flow begins to separate. The autocorrelation analyses of the surface pressure measurements also suggest that such large scale structures in the separated flow may vary in sizes as the Reynolds number increases.

Nomenclature

α	angle of attack [(°)]
c	aerofoil chord length [mm]
C_p	pressure coefficients [-]
δ	boundary layer thickness [mm]
f	frequency related to aerofoil noise [Hz]
λ^2	magnitude squared coherence [-]
ϕ_{pp}	PSD of the pressure fluctuations [dB/Hz]
ϕ_{uu}	PSD of the wake velocity [dB/Hz]
p_0	reference pressure for PSD calculations [Pa]
U_∞	free stream velocity [m/s]
U	local time-averaged velocity [m/s]
U_{rms}	local time-averaged velocity fluctuation [m/s]
Re_c	Reynolds number based on chord length [-]
x/c	streamwise distance to chord ratio [-]
x	coordinate along the streamwise direction [-]
y	coordinate along the vertical direction [-]
z	coordinate along the spanwise direction [-]
PSD	Power Spectral Density [dB/Hz]

*Research Associate, Department of Aerospace Engineering, University of Bristol.
†Ph.D. Researcher, Department of Aerospace Engineering, University of Bristol.
‡Professor of Aerodynamics and Aeroacoustics, Department of Mechanical Engineering, University of Bristol.

I. Introduction

Airfoil self-noise has attracted significant research interest for several decades due to its importance to industrial engineering applications and relevance to the health concerns of the community. This has become increasingly the case as air travels grow rapidly and regulations on the noise emission levels tighten further.[1–3] Therefore, it calls upon more research efforts and resources to better understand the noise generation mechanisms of the airfoil self-noise, and on top of such fundamental understanding, to device novel and effective strategies for noise mitigation of aircrafts and turbomachineries.

In a seminal work by Brooks *et al.*,[4] they identified five different categories of airfoil self-noise. For airfoils at moderate to high Reynolds numbers with a sharp trailing-edge, trailing-edge noise and stall noise are the primary and dominating noise sources at low and high angles of attack (*i.e.* attached and separated flow conditions), respectively. More importantly, they developed an empirical model to predict the trailing-edge noise of an airfoil based on their extensive experimental measurements of NACA 0012 airfoils. The phenomenon and underlying mechanisms of airfoil self-noise at low to moderate angles of attack has been examined extensively from the analytical,[5–8] numerical[9,10] and experimental[11–15] point of view. According to Amiet's theory,[5] the trailing-edge noise is a direct result of the scattering of turbulent structures within a boundary layer, and hence is related to both the surface pressure fluctuations and the boundary layer length scales at the airfoil trailing-edge. Moreau and Roger[8] later modified the theory to take the leading-edge scattering effects into account. More recently, Gargia and Hynes[11] and Herrig *et al.*[12] conducted detailed measurements of the surface pressure fluctuation and the spanwise correlation length close to the trailing-edge of an airfoil, in an attempt to examine and understand the correlation between the near-field dynamics and far-field radiated noise. Herrig *et al.*[12] reported that the prediction of far-field noise can be greatly improved with accurate flow field information of the near-field.

Past studies often focused on the classic airfoil profiles such as flat-plate-like[13] or NACA 0012[11,14,16] profiles, partly due to its symmetric profile shape. Nevertheless, a cambered airfoil profile is often preferred as a 'point-of-entry' in industrial design applications,[17] and since changes in the profile shape will directly modify the development of the turbulent structures in the boundary layer and their interactions with the cambered shape, it is crucial to examine and understand the airfoil self-noise from cambered airfoils as well. In fact, there have been limited studies on the detailed near-field aeroacoustic measurements for a cambered airfoil. Inspired by the fact that a more comprehensive study is desired to shed more light on the airfoil self-noise of a cambered airfoil from attached to separated flow conditions, the present study represents a preliminary effort to design and test a highly instrumented NACA 65-410 airfoil, aiming to provide an assessment of both the near-field aerodynamic and aeroacoustic characteristics. The experimental measurements will serve to both improve our fundamental understanding of the airfoil self-noise and used as benchmark cases for numerical studies.

II. Experimental setup

The experiments were conducted in the recently commissioned aeroacoustic wind tunnel facility at the University of Bristol, which has a designed lower anechoic frequency limit of 160 Hz. The closed-loop wind tunnel is fitted with an open jet with a cross-section measuring 500 mm (W) × 775 mm (L) and achieves a maximum free stream velocity of $40\,\mathrm{m\,s^{-1}}$.[15] Far-field noise can be registered by an overhead microphone arc array, equipped with 23 G.R.A.S. 40PL free field microphones, spanning across an angular range of 40° to 150°, approximately 1.75m from the center of the rectangular nozzle. A Kevlar-walled test section was designed to mount the airfoil, which allowed the test section to be permeable to acoustic waves (*i.e.* with a very small attenuation), while retaining a high level of flow uniformity, similar to the test section pioneered in the Virginia Tech stability wind tunnel.[18] This is to allow experimental measurements of the airfoil at high angles of attack without excessive deflection of the flow. Moreover, a Nidec 095E3E-FM servo motor driven by a M700 Nidec servo drive unit was connected to the airfoil side-mount structure to achieve precise control of the angle of attack (α) with an accuracy of $\pm 0.1°$. More details on the characterisation of the Kevlar-walled test section and the performance of the servo motor can be found in Mayer *et al.*[19]

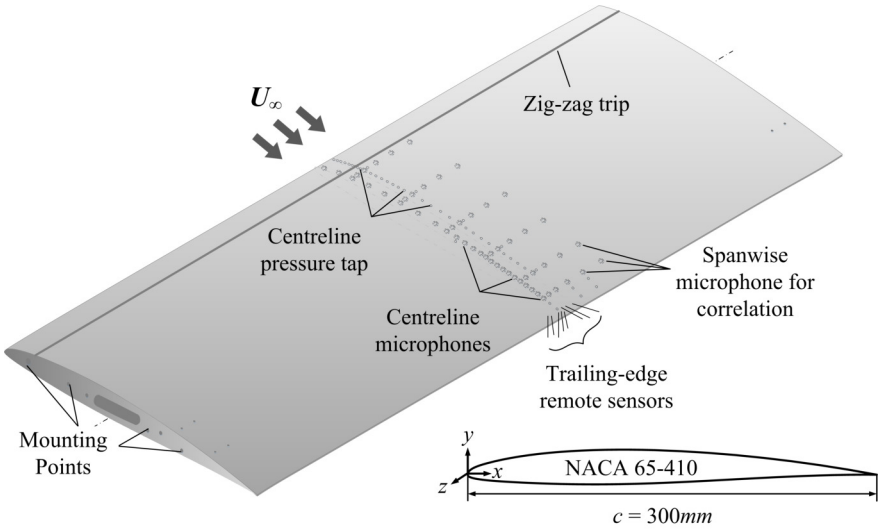

Figure 1: Schematic of the NACA 65-410 profile with surface microphones and pressure taps.

A. NACA 65-410 Airfoil

A NACA 65-410 airfoil profile, with a chord length of 300 mm was used as a representative of a highly cambered thin airfoil since the 65-family has been widely used as a 'starting point' for the design of turbine blades.[17] The airfoil has been machined from Aluminium with a hollow internal to house the necessary dynamic surface pressure transducers and pressure taps. Similar designs have been built and tested for a symmetric NACA 0012. Readers are advised to refer to the work by Mayer *et al.*[16] and Zang *et al.*[20] for more details. To allow a detailed understanding and comprehensive measurements on the near-field dynamics, the present airfoil has been populated with 80 dynamic surface pressure transducers and 65 static pressure taps, along both the suction and pressure sides, as shown in Fig. 1. The direct-sensing dynamic surface pressure transducers were situated beneath a 0.4mm pinhole to prevent any attenuation effects at high frequencies.[?, 21–24] Moreover, remote sensing microphones were employed towards the trailing-edge of the NACA 65-410 profile, due to space constraints. Such remote sensing techniques had been developed in-house and validated in the previous studies.[25, 26] Knowles FG-23629-P16 condenser microphones and Panasonic WM-61A microphones were used as the direct sensing and remote sensing transducers, respectively. All surface pressure transducers were calibrated against a G.R.A.S. 40PL free field microphone, to determine the sensitivity and phase transfer functions prior to the experiments. To achieve a turbulent boundary layer and eliminate the tonal noise from Tollmien-Schlichting instablities, zig-zag trip turbulators of 6 mm width were applied at approximately 10% of the chord.

B. Experiment and Post-processing Parameters

The experiments have been conducted at free-stream velocities of $U_\infty = 20\,\mathrm{m\,s^{-1}}$ and $U_\infty = 30\,\mathrm{m\,s^{-1}}$ to investigate the effects of Reynolds number on the near-field aerodynamic and aeroacoustic characteristics, which correspond to Reynolds numbers of $Re_c = 422{,}000$ and 633,000, respectively. The velocity profiles of the boundary layers were determined from hot-wire measurements with a Dantec 55P16 single-wire sensor probe, sampled at a rate of 2^{15} Hz. A standard Dantec 54H10 calibrator was used to calibrate the sensor probe before each run and a fourth-order polynomial was then applied to convert voltage to the velocity, with an estimated error of 1.3%. All microphones signals were simultaneously registered by National Instruments PXIe-4499 data acquisition modules at a similar sampling frequency of 2^{15} Hz, and subsequently subjected to a high-pass filter and Welch's method using a window size of 2^{13}, 50% window overlap and a resolution of 2^3 Hz, to determine the power spectral density (PSD) of the both the boundary layer velocity and surface pressure fluctuations. Last but not least, the information from the pressure taps were collected by two MicroDaq-32 pressure scanners from Chell Instruments at 1000 Hz for a duration of 60 s to obtain the time-averaged pressure coefficient distributions over the airfoil.

III. Results and Discussion

A. Static Pressure Distribution and Boundary Layer Profiles

First of all, it is important to quantify the working conditions of the experimental setup. Figure 2 shows the distributions of the static pressure coefficient for the NACA 65-410 airfoil at velocities of $20\,\mathrm{m\,s^{-1}}$ and $30\,\mathrm{m\,s^{-1}}$, respectively, for various angles of attacks (AoAs) from -2° to 15°. With reference to Fig. 2(a), the distribution follows the expected trends of a cambered airfoil with decreasing coefficients along the suction side as the angle of attack (AOA) increases, before the flow separates at approximately 12°, which then flatterns starting from near the trailing-edge region at 12°. The pressure side sees more gradual and mild variations with the changes of AoA. Similar observations can be made with a higher free stream velocity of $U_\infty = 30\,\mathrm{m\,s^{-1}}$, except that the magnitude of the pressure coefficients are consistently greater than those at $U_\infty = 20\,\mathrm{m\,s^{-1}}$, indicating a satisfactory operating condition for the present experiments.

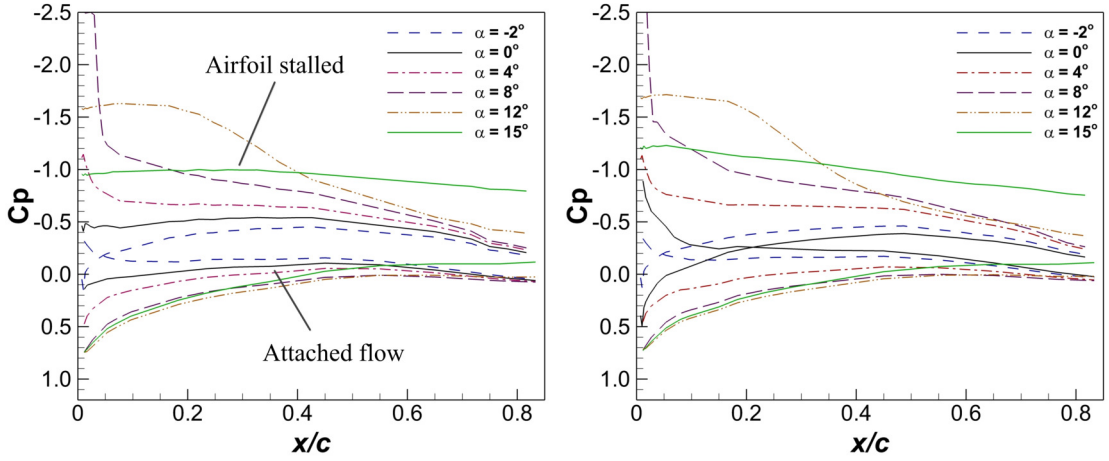

(a) U_∞ = 20m/s (b) U_∞ = 30m/s

Figure 2: Distribution of the pressure coefficients over the airfoil at (a) $U_\infty = 20\,\mathrm{m\,s^{-1}}$ and (b) $U_\infty = 30\,\mathrm{m\,s^{-1}}$ at angles of attack from α = -2° to 15°.

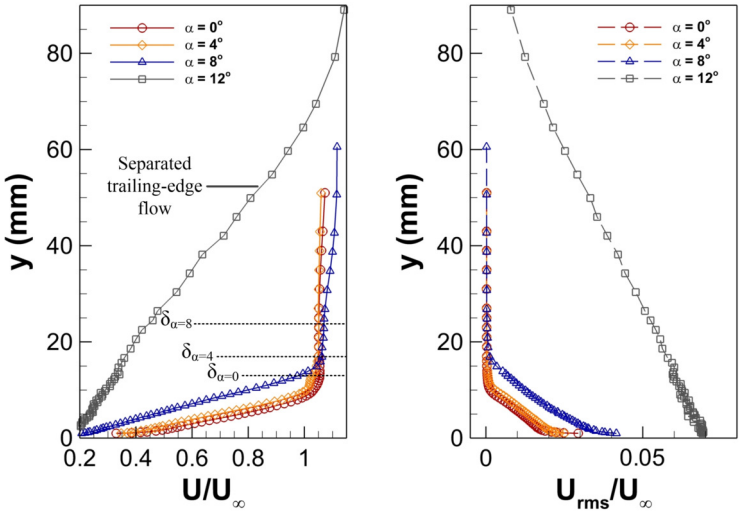

(a) Velocity Profile (b) Velocity Fluctuations

Figure 3: Boundary layer profiles of (a) normalized velocity U/U_∞ and (b) normalized velocity fluctuations U_{rms}/U_∞ of the NACA 65-410 airfoil measured at the trailing-edge for four angles of attack, α = 0°, 4°, 8° and 12°.

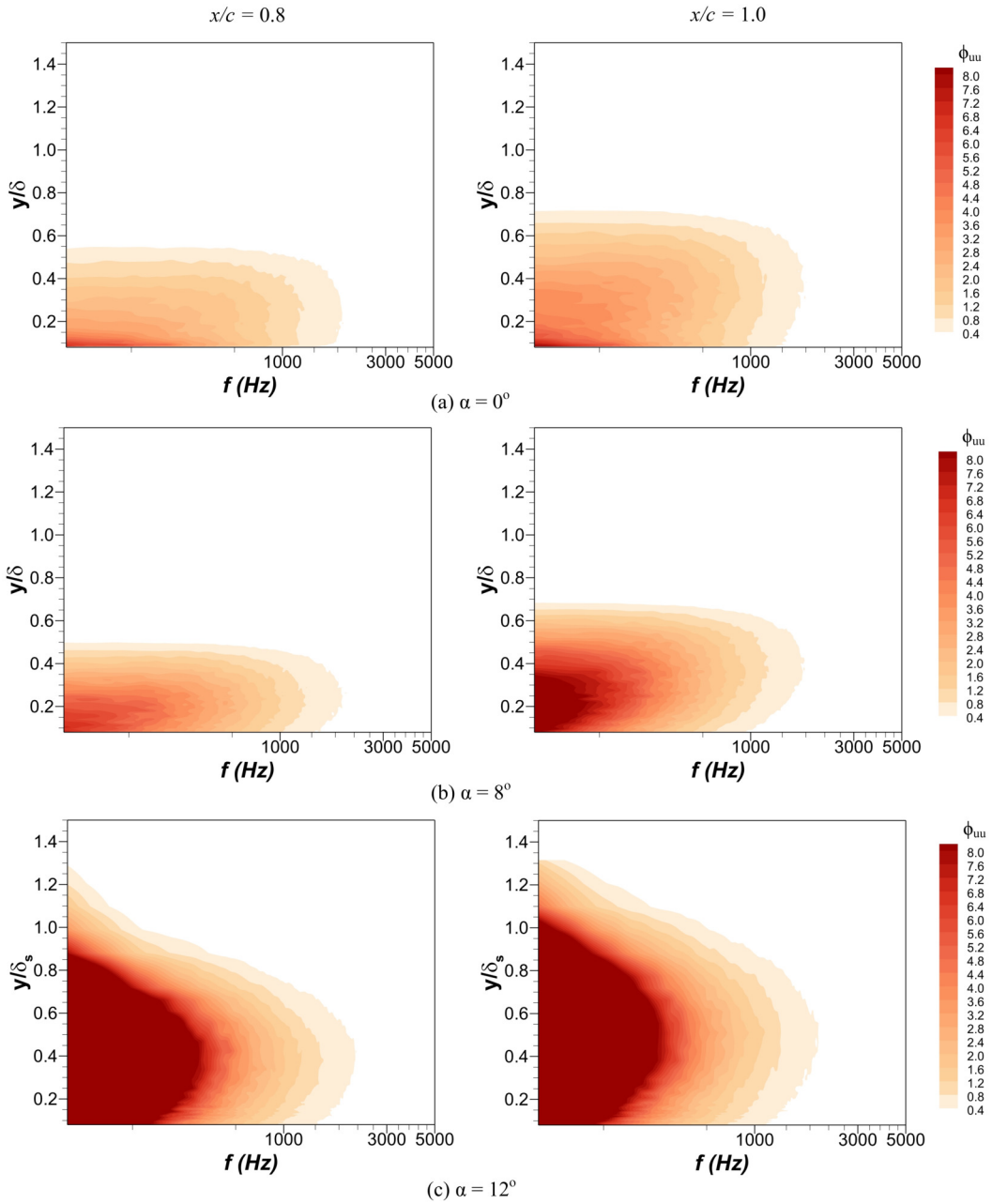

Figure 4: Contour of the power spectral density of the velocity profiles at the trailing-edge for (a) $\alpha = 0°$, (b) $\alpha = 8°$ and (c) $\alpha = 12°$ at $U_\infty = 20\,\mathrm{m\,s^{-1}}$. Note that the reference pressure of $p_0 = 20 \cdot e^{-6}$Pa has not been applied to the PSD for the present velocity measurements.

Figure 3(a) shows the boundary layer profiles measured at the trailing-edge ($x/c = 1$) of the airfoil at corresponding AoAs at $U_\infty = 20\,\mathrm{m\,s^{-1}}$. The boundary layer continues to grow from approximately $\delta = 12\,\mathrm{mm}$ at $\alpha = 0°$ to $\delta = 23\,\mathrm{mm}$ at $\alpha = 8°$ before the flow separation takes place and boundary layers can no longer to clearly defined. In addition, Fig. 3(b) shows the root mean square of the velocity fluctuations, normalized by the free-stream velocity. Note that the symbols are kept consistent with that of the velocity profile for ease of comparison. Not surprisingly, the velocity fluctuations are almost twice as high as the flow undergoes separation as compared to the attached scenarios.

The velocity fluctuations at the trailing-edge of the airfoil are examined more closely since it is directly related to both the trailing-edge and stall noise of an airfoil. The power spectral density (PSD) of the velocity fluctuations are shown in Fig. 4. As seen from the comparison between locations $x/c = 0.8$ and

$x/c = 1.0$, the PSD distributions follow closely that of the boundary layer growth. Moreover, majority of the fluctuations (hence, energy frequency contents) are identified to be very close to the surface of the airfoil, below $y/\delta = 0.6$, regardless of the angle of attack, when the flow remains attached to the airfoil. On the contrary, at higher angle of attack of $\alpha = 12°$, as the airfoil transitions to stall condition, a significant growth in the low frequency energy contents can be observed at both the $x/c = 0.8$ and $x/c = 1.0$ locations. Moreover, the velocity fluctuation PSD extends notably in the vertical direction, y, to a height comparable with the 'thickness' of the separated flow, δ_s. Here, δ_s denotes an approximation of the flow separation height from the measured velocity profile, which was determined to be $\delta_s = 90\,\text{mm}$ under the present experimental conditions. It will be demonstrated later, in Section C that these are likely associated with the large scale structures being originated and developed within the separated flow.[4]

B. Near-field Surface Pressure Fluctuations and the Reynolds Number Effect

With the results and knowledge from the boundary layer velocity measurements, the surface pressure fluctuations have been analyzed subsequently and their associated power spectral density (PSD) levels are shown in Figs. 5 and 6 to further understand the near-field aerodynamic and aeroacoustic loadings on the airfoil. Note that a reference pressure of $p_0 = 20 \cdot e^{-6}$ was used to convert the Fourier-transformed spectra to decibels (dB/Hz). Figure 5 shows the PSD of the surface pressure fluctuations along the chord-wise locations from the mid-chord, $x/c = 0.65$, to the trailing-edge, $x/c = 0.98$, as determined from both the direct and remote sensing surface pressure transducers. Note that the frequency responses from the remote sensing transducers have been truncated at approximately $f = 6$ kHz due to the loss of accuracy beyond this frequency. The PSD illustrates an expected development of the turbulent boundary layer over an airfoil, for which, as the flow convects downstream of the airfoil, the energy contents at low frequency (*i.e.* $f < 1$ kHz) increase, accompanied with a more rapid decay of the energy contents at relatively high frequencies. Such trends agree well with those observed from the NACA 0012 experiments.[16,27] Nevertheless, the increase of the energy contents at low frequencies appear to be more gradual than for the symmetric NACA 0012 airfoil, possibly due to the cambered airfoil having a different growth of the turbulent boundary layer over surface. On the other hand, when the flow separates from the airfoil surface starting from $\alpha \approx 12°$, the PSD of the surface pressure fluctuations demonstrates a monotonic decay with an almost constant gradient. Comparing the surface pressure fluctuation along the chord-wise locations, the PSD experiences a noticeable reduction from the mid-chord location toward the trailing-edge, suggesting that the flow becomes increasingly separated from the airfoil surface.

When the flow velocity increases to $U_\infty = 30\,\text{m}\,\text{s}^{-1}$, as shown in Fig. 6, the evolution of the surface pressure fluctuations from the mid-chord location to the trailing-edge are generally similar to those at $U_\infty = 20\,\text{m}\,\text{s}^{-1}$ for all the angles of attack. However, there exist several differences to be highlighted. Firstly, the magnitude of the PSD increases for all pressure measurement locations. Secondly, the decay of the PSD appears to take place at a relatively higher frequency compared to that at lower free-stream velocity, and hence lower Reynolds number (see Figs. 5(c) and 6(b)). The shift to higher frequencies signifies an increase in the energy frequency contents and the unsteady loading on the airfoil as the Reynolds number increases.

To provide more information on the scales and structures of the turbulent boundary layer close to the airfoil surface, the autocorrelation, R_{pp}, of the surface pressure fluctuations were obtained at similar chord-wise locations, *i.e.* from $x/c = 0.65$ to 0.98. The autocorrelation is calculated using standard approach as:

$$R_{p'_i p'_i}(\tau) = \frac{\overline{p'_i(t+\tau)p'_i(t)}}{p'_{i_{rms}} p'_{i_{rms}}}, \tag{1}$$

where $p'_{i_{rms}}$ is the root-mean-square of the surface pressure fluctuation. Figures 7 and 8 depict the autocorrelation of the surface pressure fluctuations for various angles of attack from $\alpha = -2°$ to 15°, at $U_\infty = 20\,\text{m}\,\text{s}^{-1}$ and $30\,\text{m}\,\text{s}^{-1}$, respectively. For brevity, the autocorrelation prior to flow separation is not presented at the higher free-stream velocity as the behavior remains largely comparable to the lower free-stream velocity case. As seen in Fig. 7 at lower angles of attack, such as $\alpha = -2°$ and 0°, the existence of dominant turbulent structures can be clearly observed at the locations immediately after the mid-chord $x/c = 0.65$, as indicated by the pair of local minimum points in the autocorrelation profile with very small temporal shift, $\tau U_\infty/c$, symmetric about the centreline.[21] The pair of local minimum diminish with downstream distance since boundary layer develops becomes fully turbulent over the airfoil, and consequently, the autocorrelation

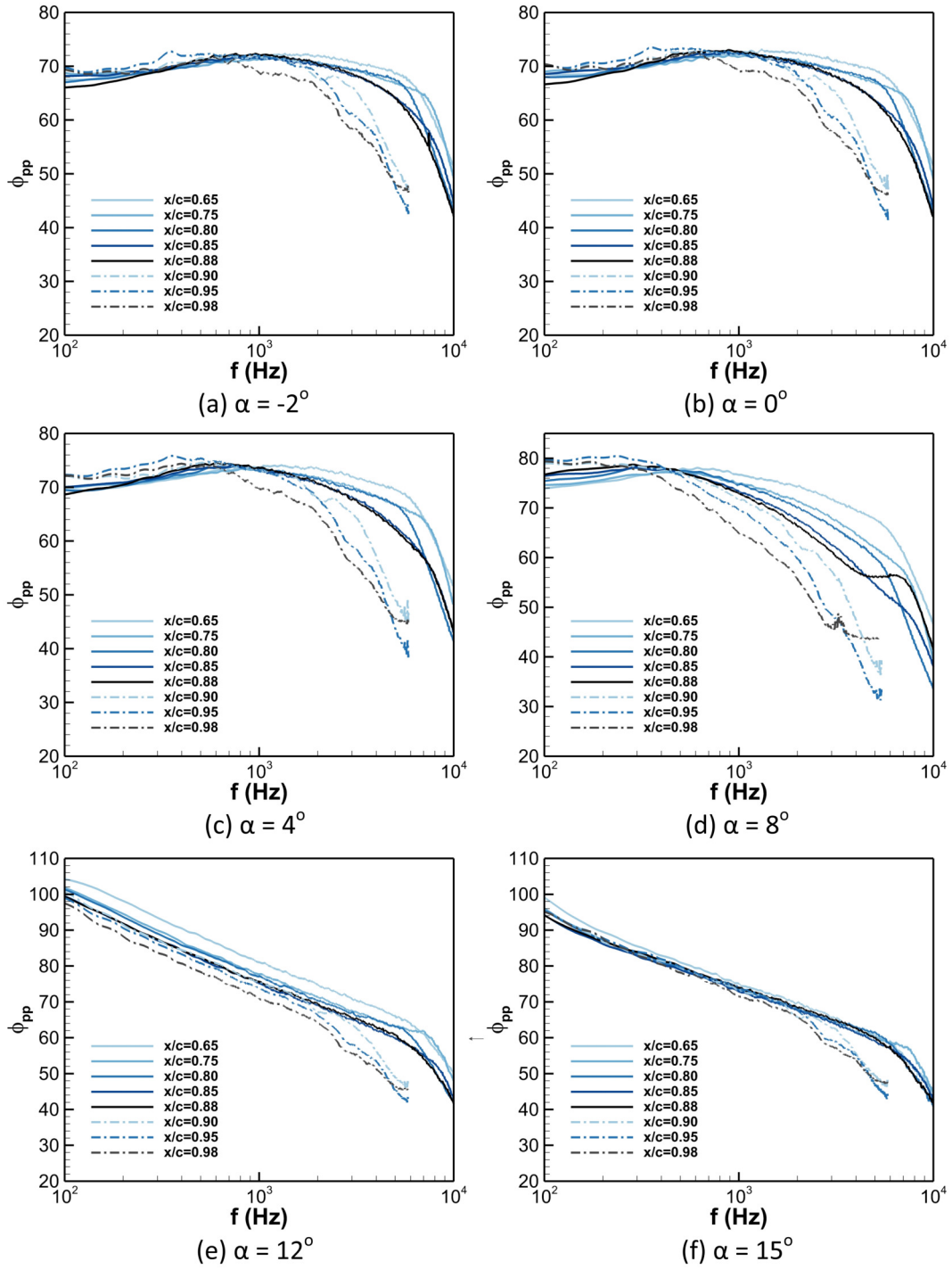

Figure 5: Power spectral density, ϕ_{pp} (dB/Hz), of the surface pressure fluctuations at several chordwise locations for angles of attack of(a) α = -2°, (b) $\alpha = 0°$, (c) $\alpha = 4°$, (d) $\alpha = 8°$, (e) $\alpha = 12°$ and (f) $\alpha = 15°$, at $U_\infty = 20\,\mathrm{m\,s^{-1}}$.

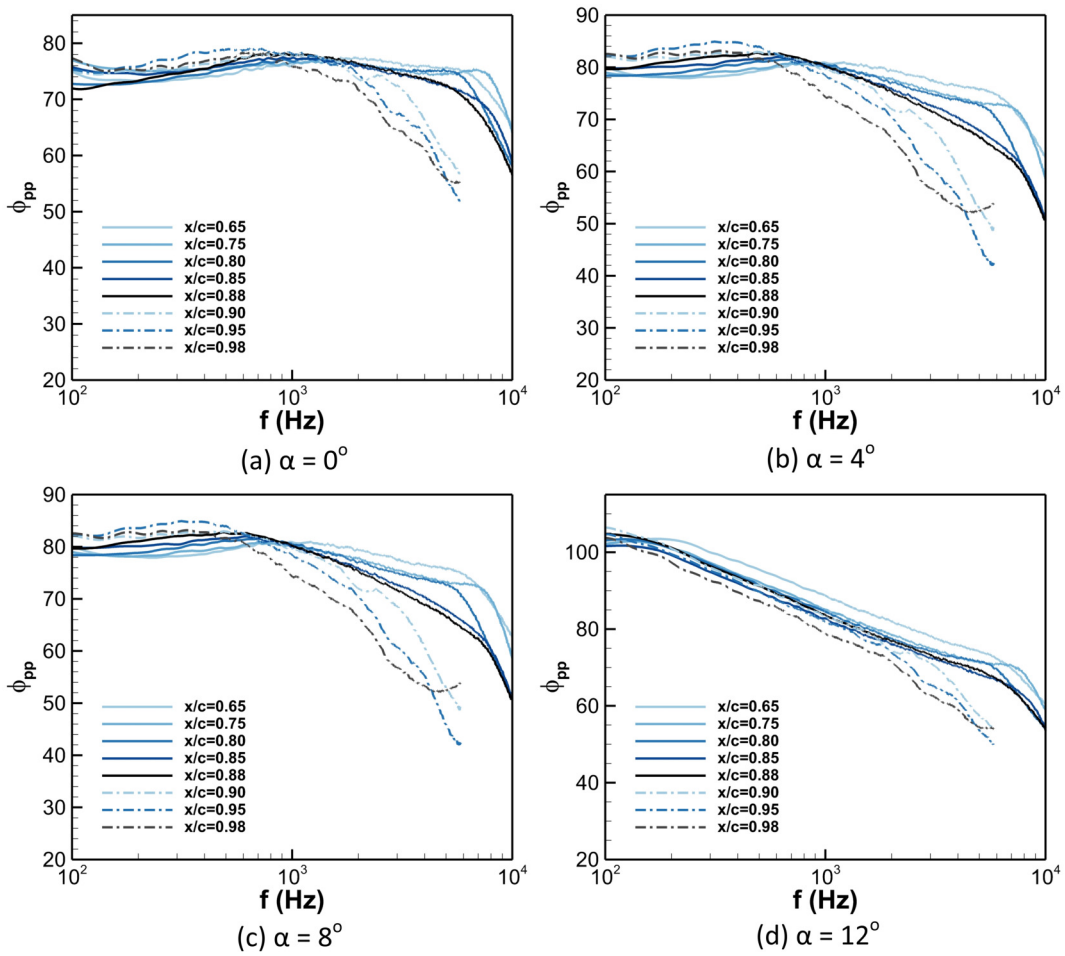

Figure 6: Power spectral density, ϕ_{pp} (dB/Hz), of the surface pressure fluctuations at several chordwise locations for angles of attack (a) $\alpha = 0°$, (b) $\alpha = 4°$, (c) $\alpha = 8°$, (d) $\alpha = 12°$, at $U_\infty = 30\,\mathrm{m\,s^{-1}}$.

profile assumes its profile shape for a developed turbulent boundary layer.[16,27] When the flow becomes separated at high angles of attack, *i.e.* $\alpha = 12°$ and $15°$, the autocorrelation profile deviates substantially from that of the developed turbulent boundary layer. It exhibits an undulating behaviour with a large amplitude and period. Increasing the free-stream velocity to $30\,\mathrm{m\,s^{-1}}$ does not vary the general trend of the autocorrelation profiles, regardless of the angle of attack. Nevertheless, it is noteworthy to highlight the differences of the autocorrelation profiles at the higher Reynolds number, under the separated flow conditions. Comparing Figs. 8 to 7(e) and (f), a higher Reynolds number leads directly to the narrowing of the autocorrelation profiles, which reach the local minimum at $\tau U_\infty/c = 0.3$ and 0.6 for $\alpha = 12°$ and $15°$ in contrast to $\tau U_\infty/c = 0.45$ and 0.75 at the lower Reynolds number. The differences in the profiles point to the possible size and periodicity differences in the flow structures of the separated flow over the airfoil.

C. Near-field Pressure and Velocity Coherence

With multiple pressure measurement locations over the chord of the airfoil, signal coherence between an individual pressure measurement point and the others over the airfoil can be determined, in order to examine the frequency-dependent flow dynamics. Figure 9 shows the coherence (γ^2) between a reference pressure measurement at $x/c = 0.88$ and the others at distinct chord-wise locations for a range of angles of attack, at free-stream velocity of $U_\infty = 20\,\mathrm{m\,s^{-1}}$. The last direct sensing micophone has been used to determine the coherence across the airfoil chord due to its more accurate frequency and phase responses during measurement. Moreover, as seen from the surface pressure fluctuation PSD results earlier, the decay of the PSD toward

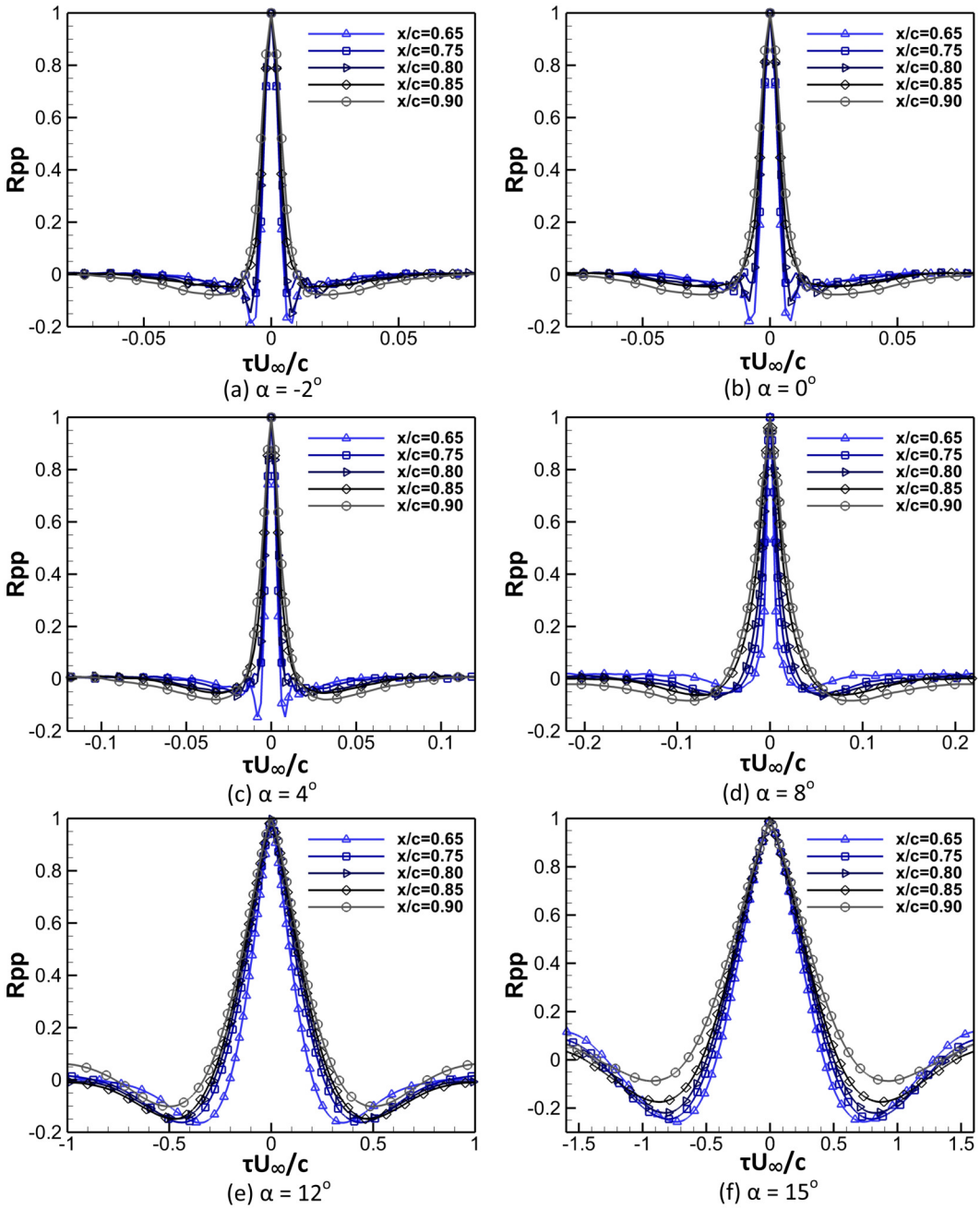

Figure 7: Autocorrelation (R_{pp}) of the surface pressure fluctuations at several chordwise locations for angles of attack of (a) α = -2°, (b) $\alpha = 0°$, (c) $\alpha = 4°$, (d) $\alpha = 8°$, (e) $\alpha = 12°$ and (f) $\alpha = 15°$, at $U_\infty = 20\,\mathrm{m\,s^{-1}}$.

high frequency tend to be more rapid for the remote sensing transducers than for the direct sensing ones. Therefore, they were not selected as the reference microphone and care should be exercised when intepreting these results. Here, the magnitude squared coherence from the surface pressure measurements is calculated as:

$$\gamma^2(f) = \frac{|\phi_{pi,pj}(f)|^2}{\phi_{pi,pi}(f)\phi_{pj,pj}(f)} \tag{2}$$

It should be mentioned that the self-coherence of the microphone has been omitted since it should always be at unity. Clearly from the results, while the pressure coherence are primarily limited to adjacent measurement locations toward the trailing-edge region at low angles of attack from $\alpha = -2°$ to 4°, it begins to extend

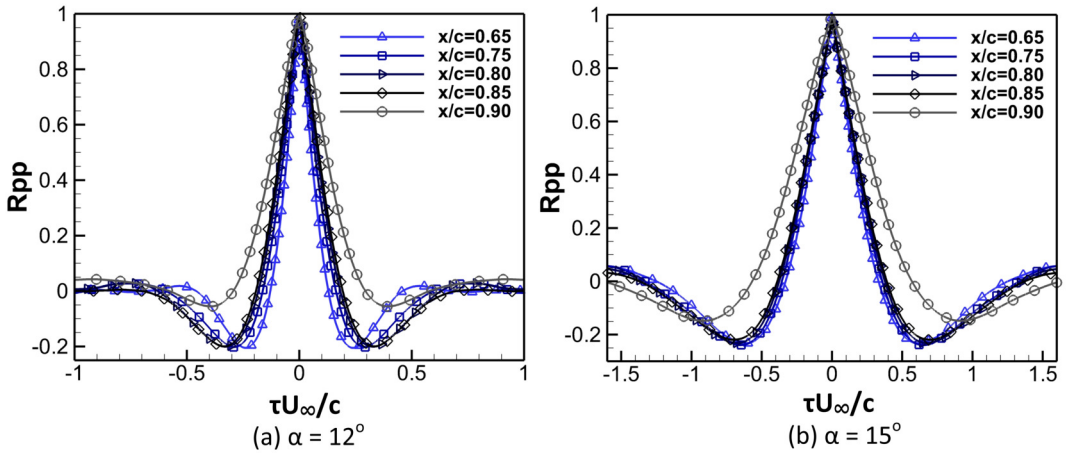

Figure 8: Autocorrelation (R_{pp}) of the surface pressure fluctuations at several chordwise locations for angles of attack of (a) $\alpha = 12°$, (b) $\alpha = 15°$, at $U_\infty = 30\,\mathrm{m\,s^{-1}}$, where the airfoil is transitioning into stall.

notably toward the leading-edge of the airfoil as α increases to 8°, suggesting that large flow structures begin to emerge, in particular at frequencies of $200\,\mathrm{Hz} < f < 400\,\mathrm{Hz}$. Recall that this region corresponds very well with that observed from the PSD of the boundary layer velocity measurements, as shown in 4. At $\alpha = 12°$, the coherence in the low frequencies seem to have spanned more than half of the airfoil chord.

Figure 10 shows the pressure–velocity (p–u) coherence at the chord-wise location of $x/c = 0.8$ for two angles of attack, $\alpha = 0°$ and 12°. The p–u coherence serves to elucidate the relation between the turbulent structures and energy contents from the boundary layer flow and those influencing the surface pressure fluctuations and helps to confirm whether the pressure coherence observed in Fig. 9 is a direct result of the turbulent boundary layers influencing the airfoil surface. As recently noted by the authors, the conventional definitions of p–u coherence and correlation can sometimes cause spurious regions of high coherence and correlation to emerge beyond the boundary layer. Therefore, the p–u coherence presented here has been normalized with the free-stream velocity as:

$$\gamma_{pu}^2(f) = \frac{|\phi_{pu}(f)|^2}{\phi_{pp}(f)U_\infty}, \tag{3}$$

Moreover, an arbitrary factor of 10^5 has been post-multiplied to the γ_{pu}^2 such that the order of magnitude is $O(\gamma_{pu}^2) \sim 1$. At $\alpha = 0°$, strong p–u coherence can be observed close to the surface up to $y/\delta = 0.4$ in the frequency range of approximately $50\,\mathrm{Hz} < f < 1000\,\mathrm{Hz}$ (see Fig. 10(a), which is very similar to the range of frequencies with elevated coherence levels identified from the surface pressure coherence calculations. This demonstrates a close relation between turbulent flow structures within the boundary layer over the airfoil and the surface pressure fluctuations exerted on the airfoil. Referring to the p–u coherence for the separated flow conditions in Fig. 10(b), the region of strong p–u coherence extends all the way to the boundary (*i.e.* thickness) of the separated flow at low frequencies.

D. Near-field to Far-field Coherence

Fig. 11 illustrates the coherence calculated between the near-field and far-field microphones located 90° above of the airfoil trailing-edge. Despite the small magnitude of the coherence often expected between near- and far-field measurements, a sharp rise in the coherence at low frequencies of $f < 500\,\mathrm{Hz}$ can be observed for at the trailing-edge when the airfoil begins to stall. This is in agreement with the near-field surface pressure coherence. Consequently, it is reasonable to argue that the airfoil noise can possibly be attributed to the development of large-scale flow structures in the separated flow over the airfoil at high angles of attack.

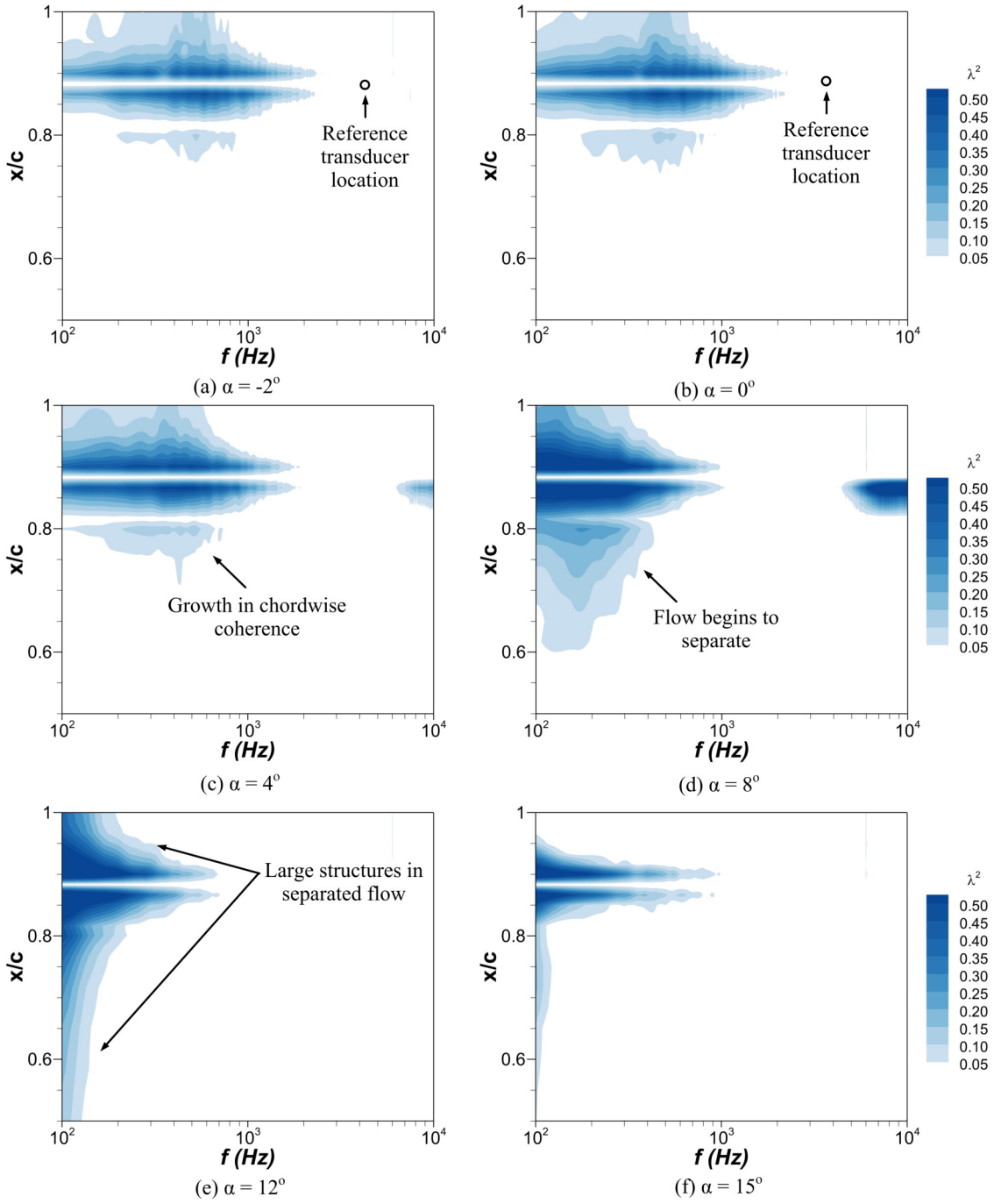

Figure 9: Near-field coherence contour map between the reference microphone at $x/c = 0.88$ and the other chord-wise microphones along the suction side of the airfoil for angles of attack of (a) α = -2°, (b) $\alpha = 0°$, (c) $\alpha = 4°$, (d) $\alpha = 8°$, (e) $\alpha = 12°$ and (f) $\alpha = 15°$, at $U_\infty = 20\,\mathrm{m\,s^{-1}}$.

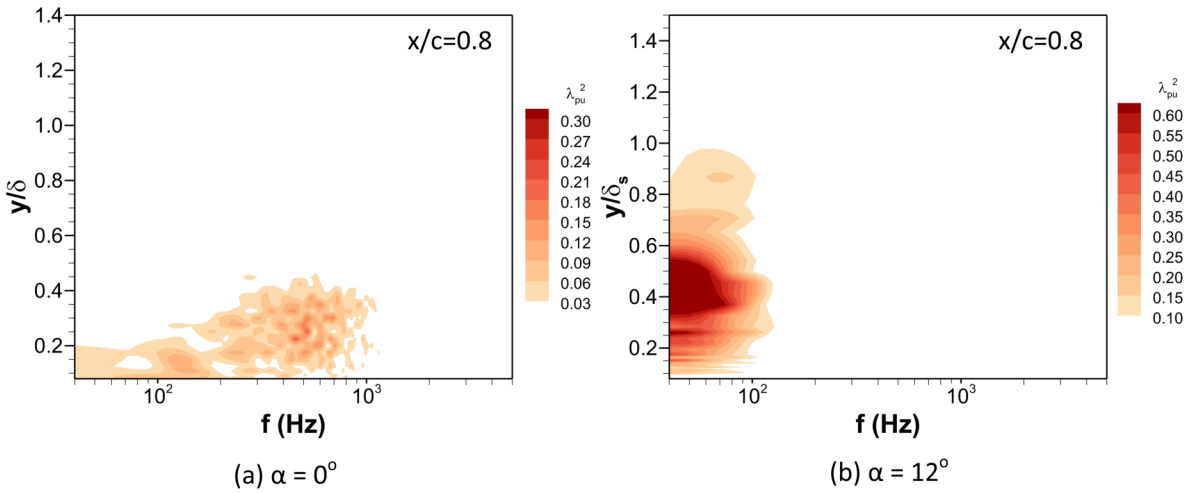

Figure 10: Pressure–velocity coherence contour map between the simultaneous velocity and surface pressure fluctuation measurements at $x/c = 0.80$ for pre-stalled angle of attack of (a) $\alpha = 0°$, and stalled angle of attack of (b) $\alpha = 12°$, at $U_\infty = 20\,\mathrm{m\,s^{-1}}$.

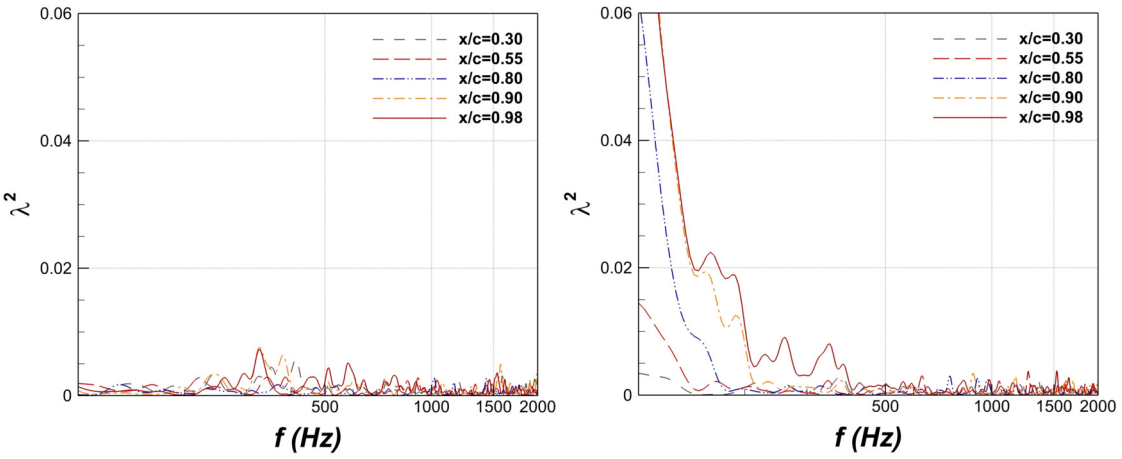

Figure 11: Near- and far-field coherence between the surface microphones at several chordwise locations and the far-field microphone located at 90° above the trailing-edge of the airfoil for angles of attack of (a) $\alpha = 4°$ and (b) $\alpha = 12°$, at $U_\infty = 20\,\mathrm{m\,s^{-1}}$.

IV. Concluding remark

A series of experiments have been conducted to examine the near-field aerodynamic and aeroacoustic characteristics of a cambered NACA 65-410 airfoil at moderate Reynolds numbers, with a range of angles of attack. Both the velocity measurements and surface pressure fluctuations have revealed clear distinctions between attached and separated flow conditions. In particular, an increase in the coherence at low frequencies along the chordwise direction of the airfoil can be observed as the flow separates from the airfoil, signifying the origination and development of large-scale structures in the separated boundary layer. This is further corroborated with the presuure–velocity coherence determined at a similar chord-wise location, where for the separated flow condition, the region of high p–u coherence extends to the entire separated boundary layer extent. More interestingly, it corresponds well to a rise in the coherence levels between the near-field pressure fluctuations and the far-field noise measurements.

Acknowledgement

The authors would like to acknowledge the financial support from the EPSRC for the present study via research grant No. EP/R010846/1.

References

[1]Jarup, L., Dudley, M. L., Babisch, W., Houthuijs, D., Swart, W., Pershagen, G.and Bluhm, G., Katsouyanni, K., Velonakis, M., Cadum, E., and Vigna-Taglianti, F., "Hypertension and Exposure to Noise near Airports (HYENA): Study design and noise exposure assessment," *Environmental Health Perspectives*, Vol. 113, No. 11, 2005, pp. 1473–1478.

[2]2Knopper, L. D. and Ollson, C. A., "Health effects and wind turbines : A review of the literature," *Environmental Health*, Vol. 10, No. 1, 2011, pp. 78–88.

[3]Nobbs, B., Doolan, C. J., and Moreau, D. J., "Characterisation of noise in house affected by wind turbine noise," *Proceedings of Acoustics 2012*, Fremantle, Australia, 2012.

[4]Brooks, T. F., Pope, D. S., and Marcolini, M. A., "Airfoil self-noise ad prediction," Nasa reference publication 1218, NASA Langley Research Center, Hampton, Virginia, United States, 1989.

[5]Amiet, R. K., "Noise due to turbulent flow past a trailing edge," *Journal of Sound and Vibration*, Vol. 47, No. 3, 1976, pp. 387 – 393.

[6]Roger, M. and Moreau, S., "Broadband self-Noise from loaded fan blades," *AIAA Journal*, Vol. 42, No. 3, 2004, pp. 536 – 544.

[7]Howe, M. S., "A review of the theory of trailing edge noise," *Journal of Sound and Vibration*, Vol. 61, No. 3, 1978, pp. 437 – 465.

[8]Moreau, S. and Roger, M., "Back-scattering correction and further extensions of Amiet's trailing-edge noise model. Part 1: Theory," *Journal of Sound and Vibration*, Vol. 286, No. 3, 2005, pp. 477 – 506.

[9]Moreau, S., Christophe, J., and Roger, M., "LES of the trailing-edge flow and noise of a NACA 0012 airfoil near stall," Proceedings of the summer program, Center for Turbulence Research, Stanford University, 2008.

[10]Wolf, W. R. and Lele, S. K., "Trailing-edge noise prediction using compressible Large Eddy Simulation and acoustic analogy," *AIAA Journal*, Vol. 50, No. 11, 2012, pp. 1637–1651.

[11]Garcia-Sagrado, A. and Hynes, T., "Wall pressure sources near an airfoil trailing edge under turbulent boundary layers," *Journal of Fluids and Structures*, Vol. 30, 2012, pp. 3–34.

[12]Herrig, A., Kamruzzaman, M., Würz, W., and Wagner, S., "Broadband airfoil trailing-edge noise prediction from measured surface pressures and spanwise length scales," *International Journal of Aeroacoustics*, Vol. 12, No. 1-2, 2013.

[13]Moreau, D. J., Doolan, C. J., Alexander, W. N., Meyer, T. W., and Devenport, W. J., "Wall-mounted finite airfoil-noise production and prediction," *AIAA Journal*, Vol. 54, No. 5, 2016, pp. 1637–1651.

[14]Zajamsek, B., Doolan, C. J., Moreau, D. J., J., F., and Prime, Z., "Experimental investigation of trailing edge noise from stationary and rotating airfoils," *Journal of Acoustical Society of America*, Vol. 141, No. 5, 2017, pp. 3291–3301.

[15]Mayer, Y. D., Kamliya Jawahar, H., Szöke, M., Showkat Ali, S. A., and Azarpeyvand, M., "Design and performance of an aeroacoustic wind tunnel facility at the University of Bristol," *Applied Acoustics*, Vol. 155, 2019, pp. 358 – 370.

[16]Mayer, Y. D., Zang, B., and Azarpeyvand, M., "Aeroacoustic characteristics of a NACA 0012 airfoil for attached and stalled flow conditions," *25th AIAA/CEAS Aeroacoustics Conference*, Delft, Netherland, 2019.

[17]Westphal, W. R. and Godwin, W. R., "Comparison of NACA 65-series compressor-blade pressure distributions and performance in a rotor and in cascade," National advisory committee for aeronautics, United States, 1951.

[18]Devenport, W. J., Burdisso, R. A., Borgoltz, A., Ravetta, P. A., Barone, M. F., Brown, K. A., and Morton, M. A., "The Kevlar-walled anechoic wind tunnel," *Journal of Sound and Vibration*, Vol. 332, No. 17, 2013, pp. 3971 – 3991.

[19]Mayer, Y. D., Zang, B., and Azarpeyvand, M., "Design of a Kevlar-Walled test section with dynamic turntable and aeroacoustic investigation of an oscillating airfoil," *25th AIAA/CEAS Aeroacoustics Conference*, Delft, Netherland, 2019.

[20]Zang, B., Mayer, Y. D., and Azarpeyvand, M., "An experimental investigation on the mechanism of Tollmien-Schlichting waves for a NACA 0012 aerofoil," *25th AIAA/CEAS Aeroacoustics Conference*, Delft, Netherland, 2019.

[21]Showkat Ali, S. A., Azarpeyvand, M., and Ilário da Silva, C. R., "Trailing-edge flow and noise control using porous treatments," *Journal of Fluid Mechanics*, Vol. 850, 2018, pp. 83–119.

[22]Szöke, M., Fiscaletti, D., and Azarpeyvand, M., "Effects of inclined transverse jets on trailing-edge noise generation," *Physics of Fluids*, Vol. 30, 2018, 085110.

[23]Abbas, A., Azarpeyvand, M., Dehghan, A. A., Szöke, M., and Maryami, R., "Trailing-edge flow manipulation using streamwise finlets," *Journal of Fluid Mechanics*, Vol. 870, 2019, pp. 617 – 650.

[24]Kamliya Jawahar, H., Showkat Ali, S. A., Azarpeyvand, M., and Ilário da Silva, C. R., "Aerodynamic and aeroacoustic performance of high-lift airfoil fitted with slat cove fillers," *Aerospace Science and Technology*, Vol. In-press, 2020.

[25]Liu, X., Showkat Ali, S. A., and Azarpeyvand, M., "On the application of trailing-edge serrations for noise control from tandem airfoil configurations," *23th AIAA/CEAS Aeroacoustics Conference*, Denver, Colorado, United States, 2017.

[26]Elsahhar, E., Showkat Ali, S. A., Raf, T., and Azarpeyvand, M., "An experimntal investigation of the effect of bluff body bluntness factor on wake-vortex noise generation," *24th AIAA/CEAS Aeroacoustics Conference*, Atlanta, Geogia, United States, 2018.

[27]Garcia-Sagrado, A., *Boundary layer and trailing edge noise sources*, Ph.D. thesis, 2008.